



Significant role of first-principles electron-phonon coupling in the electronic and thermoelectric properties of LiZnAs and ScAgC semiconductors

Vinod Kumar Solet  and Sudhir K. Pandey 

School of Mechanical and Materials Engineering, Indian Institute of Technology Mandi, Kamand 175075, India

(Dated: June 17, 2025)

The half-Heusler (hH) compounds are currently considered promising thermoelectric (TE) materials due to their favorable thermopower and electrical conductivity. Accurate estimates of these properties are therefore highly desirable and require a detailed understanding of the microscopic mechanisms that govern transport. To enable such estimations, we carry out comprehensive first-principles computations of one of the primary factors limiting carrier transport, namely the electron-phonon (e - ph) interaction, in representative hH semiconductors such as LiZnAs and ScAgC. Our study first investigates the e - ph renormalization of electronic dispersion based on the non-adiabatic Allen–Heine–Cardona theory. We then solve the Boltzmann transport equation (BTE) under multiple relaxation-time approximations (RTAs) to evaluate the carrier transport properties. Phonon-limited electron and hole mobilities are comparatively assessed using the linearized self-energy and momentum RTAs (SERTA and MRTA), and the exact or iterative BTE (IBTE) solutions within e - ph coupling. Electrical transport coefficients for TE performance are also comparatively analyzed under the constant RTA (CRTA), SERTA, and MRTA schemes. The lattice thermal conductivity, determined from phonon-phonon interaction, is further reduced through nanostructuring techniques. The bulk LiZnAs (ScAgC) compound achieves the highest figure of merit (zT) of ~ 1.05 (0.78) at 900 K with an electron doping concentration of 10^{18} (10^{19}) cm^{-3} under the MRTA scheme. This value significantly increases to ~ 1.53 (1.0) for a 20 nm nanostructured sample. The remarkably high zT achieved through inherently present phonon-induced electron scattering and the grain-boundary effect in semiconductors opens a promising path for discovering highly efficient and accurate hH materials for TE technology.

I. INTRODUCTION

The half-Heusler (hH) semiconductors have received significant attention as promising thermoelectric (TE) materials for medium- and high-temperature clean energy-harvesting technology [1–9]. The efficiency of TE materials is given by the dimensionless figure of merit $zT = \sigma S^2 T / \kappa$, where σ is the electrical conductivity, S is the Seebeck coefficient, T is the temperature, and $\kappa = (\kappa_e + \kappa_{ph})$ is the total thermal conductivity, comprising the electronic (κ_e) and lattice (κ_{ph}) contributions [10]. The hH materials usually exhibit very promising electron transport properties, particularly high σ and S values, as seen in compounds like ZrNiSn and cobalt-based hH alloys, which contribute to a high TE power factor σS^2 [7, 11–13]. Interestingly, hH materials also exhibit a wide range of κ_{ph} , making these compounds attractive for various energy-related applications [9, 11, 14]. However, the inherently 2–4 times higher κ values of these compounds compared to other cutting-edge TEs [11] poses a major challenge to achieving high TE conversion efficiency [15–17]. While maximizing the zT value by tweaking electrical coefficients (σ , S , κ_e) is often complex and limited by their interrelation, and thus reducing κ_{ph} is considered a more effective route without significantly affecting the other factors [18, 19]. Several promising approaches such as grain boundary engineering and doping engineering have been proposed over the years to lower κ in hH materials [20–23]. At the same time, understanding the microscopic mechanisms for accurate estimation of electric transport coefficients is also highly desirable for predicting favorable TE

materials. Therefore, the microscopic physics underlying both particles (electron and phonon) transport needs to be well understood [24], not only for fundamental scientific research but also for advancing practical TE device applications.

From the well-known relation $\sigma = ne\mu$ [25], where n is the carrier concentration, e is the charge of carrier, and μ is the carrier mobility, a more accurate zT value effectively depends on the precise determination of mobility. In first principles density functional based calculations, obtaining transport properties such as μ and κ is quite challenging, as it requires a detailed understanding of how particles are scattered by each other or by other particles [26]. These scattering mechanisms can be understood from the Boltzmann transport theory by describing carriers as wave packets that propagate according to semi-classical equations of motion between two successive scattering events [27, 28]. For mid- and high-T TE applications, the μ value is significantly affected by electron-phonon (e - ph) scattering in semiconductors [29, 30]. e - ph coupling also plays a crucial role in transport properties calculation by reshaping the electronic dispersion, i.e., the T-dependent renormalization of band structure [29, 31–34]. First-principles e - ph interaction (EPI) calculations demonstrate that electron lifetime varies significantly with electron energy and carrier concentration [8, 29], suggesting the need to go beyond the commonly used constant relaxation time approximation (CRTA) to effectively screen and optimize material’s properties. Therefore, analyzing microscopic EPI mechanisms in hH materials is favorable for accurately obtaining the electrical components of TE materials. On the other hand, phonon-phonon interaction (PPI) dominates in the thermal transport of semiconductors [27]. In TE materials, the electron mean-free-path (MFP) is much smaller than the phonon MFP [35, 36]. Therefore, the use of nanostructuring techniques with grain sizes above

* vsolet5@gmail.com

† sudhir@iitmandi.ac.in

the electron MFP can be the most efficient way to reduce κ_{ph} [37]. Thus, combining the effects of EPI on electrical transport and PPI on phonon transport can effectively aid in accurately identifying and designing hH materials for TE applications.

The hH materials, composed of one main-group element and two transition metals, offer a wide range of tunability, among which 18 valence electrons systems have gained considerable interest for waste-heat recovery applications [7, 17, 38]. The quest to enhance hH material's properties for TE applications can proceed either by doping existing compounds [16] or by identifying novel materials with superior properties. Systems with 8 valence electrons fit well into the latter category, as they have received relatively less attention for TE applications compared to 18 valence electron-based alloys [7, 39–42]. We have identified from best literature survey that most existing studies on 8 valence electron-based hH alloys have only considered CRTA to estimate the TE transport coefficients [39, 41–48]. Previous studies on TE materials show that the energy-dependent electron relaxation time within EPI significantly affects both σ and κ_e compared to values obtained using CRTA [37, 49]. More importantly, the Seebeck coefficient is also impacted and matches experimental results more closely within EPI [37]. Similarly, for 18 valence electron-based compounds, the study by Samsonidze *et al.* [8] highlights a significant difference between CRTA and phonon-limited charge transport parameters in both n-type and p-type samples. Therefore, more reliable predictions of charge transport properties for 8 valence electron-based hH materials using advanced many-body *e-ph* scattering mechanisms remains a largely unexplored and promising research area in TE applications.

To fulfill this research gap, we have studied the effect of *e-ph* coupling on electronic band structure and electrical transport properties of two 8 valence electron-based LiZnAs and ScAgC hH materials using advanced *ab initio* calculations based on many-body perturbation theory (MBPT). The zero-point renormalization (ZPR) and T dependence band gaps upto 900 K using the EPI calculations within the Allen–Heine–Cardona (AHC) theory have been analyzed. The ZPR corrections to the density functional theory (DFT) based band gaps of ~ 0.6 and 0.45 eV are obtained to be around 15–16 and 36–39 meV for LiZnAs and ScAgC, respectively. We then employ the linearized Boltzmann transport equation (BTE) under self-energy and momentum relaxation-time approximations (RTAs) [SERTA and MRTA], as well as the iterative BTE (IBTE) solutions, to calculate the T-dependent electron and hole mobilities (μ_e and μ_h). The calculated room-temperature μ_e (μ_h) values are ~ 6500 (160), 12560 (213), and 17000 (195) $\text{cm}^2 \text{V}^{-1} \text{s}^{-1}$ for LiZnAs and ~ 4010 (50), 9440 (70), and 8510 (54) $\text{cm}^2 \text{V}^{-1} \text{s}^{-1}$ for ScAgC, from SERTA, MRTA and IBTE, respectively. The significantly higher μ_e compared to μ_h in both hH materials clearly indicates dominant n-type conduction over p-type.

Furthermore, the T-dependent values of S, σ and κ_e are significantly affected by the choice of RTAs such as constant RTA (CRTA), and EPI-based SERTA and MRTA. To estimate the zT , κ_{ph} is calculated using PPI and is further reduced by considering grain size effects within nanostructuring

techniques. Among the RTAs, the maximum zT is found to be around ~ 1.05 (0.78) for an electron doping levels of 10^{18} (10^{19}) cm^{-3} under MRTA for LiZnAs (ScAgC). These values are further increased to be around ~ 1.53 (1.0) when a grain size of 20 nm, within phonon-boundary scattering, is considered. These results highlight the significant role of different electron and phonon scattering mechanisms in achieving more accurate and high zT values (grater than 1) in LiZnAs and ScAgC hH materials. We hope this study provides valuable direction for guiding the discovery of novel highly efficient 8 valence electron-based hH compounds.

II. THEORY AND COMPUTATIONAL DETAILS

The starting point for our first-principles MBPT calculations is the DFT, which provides the Kohn-Sham (KS) orbital energies (ϵ_{nk}) and wave functions. We use density functional perturbation theory (DFPT) to obtain phonon responses such as interatomic force constants and eigenfrequencies, followed by the perturbation potentials used to compute the *e-ph* self-energy within MBPT [33, 50–52]. We perturb all atoms in the primitive unit cell along all three directions to compute the force constants using DFPT. All *ab initio* based EPI calculations are carried out using the Perdew-Burke-Ernzerhof (PBE) functional [53] in pseudo-potentials based Abinit software [54, 55], with a kinetic energy cutoff of 40 Hartree applied for the truncation of plane-wave basis set. The approach implemented in Abinit, as thoroughly described in Refs. [33, 52, 56, 57], achieves performance comparable to that of Wannier-based packages, without requiring the use of Wannier functions.

We estimate the ZPR correction of the electronic states, as well as its T-dependent variations, using the AHC formalism based on *e-ph* scattering calculations [32, 33, 56, 57]. Both the *on-the-mass-shell* (OTMS) and the renormalization factor included in the linearized quasiparticle equation (LQE) methods are employed to obtain the renormalized electronic eigenenergies. In our AHC calculations, the Debye-Waller (DW) self-energy is evaluated within the rigid-ion approximation, neglecting the non-diagonal DW terms [32, 34, 56, 57], while the Fan self-energy is solved using a non-adiabatic approach [33, 34]. A Γ centered $16 \times 16 \times 16$ \mathbf{k} -mesh and $8 \times 8 \times 8$ \mathbf{q} -mesh are used to obtain the ground-state electronic density and to perform DFPT phonon computations, respectively. These scattering potentials are Fourier interpolated onto a dense $48 \times 48 \times 48$ sampling in \mathbf{q} -space, while the corresponding finer Bloch states are obtained on a similar grid in \mathbf{k} -space via a non-self consistent calculation.

Accurate mobility calculations must involve the large sampling density of electron and phonon wavevectors (\mathbf{k} and \mathbf{q}) [37]. Thus, the computed *e-ph* scattering potentials on $8 \times 8 \times 8$ \mathbf{q} -mesh are Fourier interpolated onto $144 \times 144 \times 144$ \mathbf{q} grid mesh. Similarly, the large Bloch states are estimated through non-self consistent field calculations at $144 \times 144 \times 144$ \mathbf{k} points grid. The KS states used in the *e-ph* self-energy calculations for determining the carrier lifetimes are selected upto 1.0 (0.3) eV and 0.53 (0.3) eV above (below) the

conduction (valence) band minima (maxima) when electron (hole) mobility is accurately computed in LiZnAs and ScAgC, respectively. A small electron (hole) doping of 10^{15} cm^{-3} in the conduction (valence) band region is used to obtain the intrinsic mobility within electron BTE.

For lattice thermal transport, the κ_{ph} is estimated using the Phono3py program in supercell approach, which solves the phonon BTE based on three-phonon interactions (PPI) [58]. A $2 \times 2 \times 2$ supercell (including interactions only upto third-nearest neighbors for anharmonic third-order force constants) is constructed using the finite atomic displacement method, and the resulting forces on these supercells are calculated using the Abinit software. A plane wave energy cutoff of 25 Hartree, a $4 \times 4 \times 4$ \mathbf{k} -point mesh, and a force convergence criteria of 5×10^{-8} Hartree/Bohr are employed in these force calculations. Furthermore, using the second- and third-order force constants, the Brillouin zone for phonon wave vectors is integrated using a $23 \times 23 \times 23$ \mathbf{q} -point grid to solve the κ_{ph} equation within single-mode relaxation-time approximation [58]. Finally, the κ_{ph} is also evaluated by considering additional phonon-boundary scattering effects.

In a semiconductor, the mobility is directly related to the steady-state electric current and the electric field \mathbf{E} [30]. It can be obtained by taking the derivative of current with respect to the electric field, which can be written within the Boltzmann transport formalism as [30],

$$\mu_{e,\alpha\beta} = -\frac{\sum_{n \in \text{CB}} \int d\mathbf{k} v_{n\mathbf{k},\alpha} \partial_{E_\beta} f_{n\mathbf{k}}}{\sum_{n \in \text{CB}} \int d\mathbf{k} f_{n\mathbf{k}}^0} \quad (1)$$

The summations are considered for states only in the conduction bands for electron mobility ($\mu_{e,\alpha\beta}$) calculation, and ∂_{E_β} refers to $\partial/\partial E_\beta$. A similar expression, where the summation is restricted to states in the valence bands, gives the hole mobility. The band velocity $v_{n\mathbf{k},\alpha}$ is defined by the electron eigenvalue $\varepsilon_{n\mathbf{k}}$ for state $|n\mathbf{k}\rangle$, with $\hbar^{-1} \partial \varepsilon_{n\mathbf{k}} / \partial k_\alpha$. The presence of an electric field causes a deviation from the equilibrium occupation number, i.e., the Fermi-Dirac distribution $f_{n\mathbf{k}}^0$ to a nonequilibrium distribution function $f_{n\mathbf{k}}$ [25]. The indices α and β run over the three Cartesian directions (x , y , and z). In order to compute mobility in Eq. (1), we need to obtain $\partial_{E_\beta} f_{n\mathbf{k}}$, which is the linear response of $f_{n\mathbf{k}}$ to the \mathbf{E} and can be derived starting from the electron BTE as [30],

$$\begin{aligned} (-e)\mathbf{E} \cdot \frac{1}{\hbar} \frac{\partial f_{n\mathbf{k}}}{\partial \mathbf{k}} &= \frac{2\pi}{\hbar} \sum_{m\nu} \int \frac{d\mathbf{q}}{\Omega_{\text{BZ}}} |g_{mn\nu}(\mathbf{k}, \mathbf{q})|^2 \\ &\times \left\{ (1 - f_{n\mathbf{k}}) f_{m\mathbf{k}+\mathbf{q}} \delta(\varepsilon_{n\mathbf{k}} - \varepsilon_{m\mathbf{k}+\mathbf{q}} + \hbar\omega_{\mathbf{q}\nu}) (1 + n_{\mathbf{q}\nu}) \right. \\ &\quad + (1 - f_{n\mathbf{k}}) f_{m\mathbf{k}+\mathbf{q}} \delta(\varepsilon_{n\mathbf{k}} - \varepsilon_{m\mathbf{k}+\mathbf{q}} - \hbar\omega_{\mathbf{q}\nu}) n_{\mathbf{q}\nu} \\ &\quad - f_{n\mathbf{k}} (1 - f_{m\mathbf{k}+\mathbf{q}}) \delta(\varepsilon_{n\mathbf{k}} - \varepsilon_{m\mathbf{k}+\mathbf{q}} - \hbar\omega_{\mathbf{q}\nu}) (1 + n_{\mathbf{q}\nu}) \\ &\quad \left. - f_{n\mathbf{k}} (1 - f_{m\mathbf{k}+\mathbf{q}}) \delta(\varepsilon_{n\mathbf{k}} - \varepsilon_{m\mathbf{k}+\mathbf{q}} + \hbar\omega_{\mathbf{q}\nu}) n_{\mathbf{q}\nu} \right\} \quad (2) \end{aligned}$$

The left term of Eq. (2) denotes the non-collision term of BTE in a uniform and constant electric field, i.e., in the absence of magnetic field and temperature gradients. On the other hand, the right side represents the change in the distribution function due to e - ph scattering into and out of the state

$|n\mathbf{k}\rangle$, via emission or absorption of phonons with branch index ν , wave vector \mathbf{q} , and frequency $\omega_{\mathbf{q}\nu}$. $n_{\mathbf{q}\nu}$ is the Bose-Einstein occupation number. The matrix elements $g_{mn\nu}(\mathbf{k}, \mathbf{q})$ represents the e - ph probability amplitude when an electron scatters from an initial state $|n\mathbf{k}\rangle$ to final state $|m\mathbf{k} + \mathbf{q}\rangle$ via phonon $|\mathbf{q}\nu\rangle$, as computed from DFPT [29]. Finally, by taking the derivatives of Eq. (2) with respect to \mathbf{E} , the explicit expression of $\partial_{E_\beta} f_{n\mathbf{k}}$ can be estimated,

$$\begin{aligned} \partial_{E_\beta} f_{n\mathbf{k}} &= e \frac{\partial f_{n\mathbf{k}}^0}{\partial \varepsilon_{n\mathbf{k}}} v_{n\mathbf{k},\beta} \tau_{n\mathbf{k}}^0 + \frac{2\pi}{\hbar} \tau_{n\mathbf{k}}^0 \sum_{m\nu} \int \frac{d\mathbf{q}}{\Omega_{\text{BZ}}} |g_{mn\nu}(\mathbf{k}, \mathbf{q})|^2 \\ &\times \left[(1 - f_{n\mathbf{k}}^0 + n_{\mathbf{q}\nu}) \delta(\varepsilon_{n\mathbf{k}} - \varepsilon_{m\mathbf{k}+\mathbf{q}} + \hbar\omega_{\mathbf{q}\nu}) \right. \\ &\quad \left. + (f_{n\mathbf{k}}^0 + n_{\mathbf{q}\nu}) \delta(\varepsilon_{n\mathbf{k}} - \varepsilon_{m\mathbf{k}+\mathbf{q}} - \hbar\omega_{\mathbf{q}\nu}) \right] \partial_{E_\beta} f_{m\mathbf{k}+\mathbf{q}} \quad (3) \end{aligned}$$

where the relaxation time is defined as,

$$\begin{aligned} \frac{1}{\tau_{n\mathbf{k}}^0} &= \frac{2\pi}{\hbar} \sum_{m\nu} \int \frac{d\mathbf{q}}{\Omega_{\text{BZ}}} |g_{mn\nu}(\mathbf{k}, \mathbf{q})|^2 \\ &\times \left[(1 - f_{m\mathbf{k}+\mathbf{q}}^0 + n_{\mathbf{q}\nu}) \delta(\varepsilon_{n\mathbf{k}} - \varepsilon_{m\mathbf{k}+\mathbf{q}} - \hbar\omega_{\mathbf{q}\nu}) \right. \\ &\quad \left. + (f_{m\mathbf{k}+\mathbf{q}}^0 + n_{\mathbf{q}\nu}) \delta(\varepsilon_{n\mathbf{k}} - \varepsilon_{m\mathbf{k}+\mathbf{q}} + \hbar\omega_{\mathbf{q}\nu}) \right]. \quad (4) \end{aligned}$$

Equation (3) is the linearized BTE, which needs to be solved self-consistently for $\partial_{E_\beta} f_{n\mathbf{k}}$, and is commonly referred to as the IBTE. A simple approach can be considered in which only the first term on the right-hand side of Eq. (3) is used, meaning the sum term is neglected. With this consideration, one can estimate the variation $\partial_{E_\beta} f_{n\mathbf{k}}$ without solving it iteratively. In this approximation, the relaxation time $\tau_{n\mathbf{k}}^0$ is directly associated with the imaginary part of the Fan-Migdal electron self-energy via $(\tau_{n\mathbf{k}}^0)^{-1} = 2\text{Im}\Sigma_{n\mathbf{k}}^{\text{FM}}$ [37, 52], which gives the lifetime of the charged quasiparticle excitations due to EPI. The approximation involving the omission of the integral in Eq. (3) is thus referred to as the SERTA. The mobility in Eq. (1) can therefore be further updated as,

$$\mu_{e,\alpha\beta} = -\frac{e}{n_e \Omega} \sum_{n \in \text{CB}} \int \frac{d\mathbf{k}}{\Omega_{\text{BZ}}} \frac{\partial f_{n\mathbf{k}}^0}{\partial \varepsilon_{n\mathbf{k}}} v_{n\mathbf{k},\alpha} v_{n\mathbf{k},\beta} \tau_{n\mathbf{k}}^0. \quad (5)$$

where n_e is the electron density, and Ω and Ω_{BZ} are the volumes of the crystalline unit cell and first Brillouin zone, respectively. A more accurate approximation is the MRTA, which also accounts for the relative change in electron velocity during each scattering process [30]. Therefore, by multiplying the term $(1 - \hat{\mathbf{v}}_{n\mathbf{k}} \cdot \hat{\mathbf{v}}_{m\mathbf{k}+\mathbf{q}})$ in the summation of Eq. (4), and using this lifetime in Eq. (5), a more refined estimate of $\mu_{e,\alpha\beta}$ within MRTA framework is obtained.

Once the electron energy dependent lifetime $\tau_{n\mathbf{k}}^0$ is obtained, all three electrical components of TE materials such as S , σ , and κ_e are easily estimated within the electron BTE [37]. Furthermore, the complete formulation for the evaluation of electron and phonon transport properties relevant to TE materials can be found in Refs. [37, 43, 58, 59].

III. RESULTS AND DISCUSSION

A. Electron-phonon renormalization of electronic structure

Since band gap information is crucial for most T-dependent transport phenomena, understanding the renormalization of the electronic band gap is essential for high-T TE applications. In this work, T dependence of the band gap is obtained using the OTMS and LQE approaches, both of which are formulated within the non-adiabatic AHC formalism [33]. As stated by Poncé *et al.* [33], only the non-adiabatic version of the AHC equations can be reliably used when computing the ZPR for infrared-active (IR-active) materials. In our study, the calculated non-zero Born effective charges for atoms in both LiZnAs and ScAgC hH materials indicate that these compounds exhibit IR activity. This justifies the use of the non-adiabatic ZPR formulation in our calculations.

In this way, the band gap using the PBE functional is calculated to be ~ 0.6 eV for LiZnAs and ~ 0.45 eV for ScAgC, both being direct at the Γ -point and consistent with previous studies [43, 60]. Compared to OTMS, the LQE approach includes an additional factor accounting for the quasiparticle (QP) spectral weight $Z_{nk}(T)$ [37]. It is observed in Table I for both approaches that the band gap decreases with increasing T, which can be explained by its relationship with T as described by the Varshni equation [29]. Due to zero-point lattice vibrations, DFT gaps are decreased to be ~ 0.585 eV (for LiZnAs) and $0.417\text{--}0.42$ eV (for ScAgC). The ZPR is defined as the difference between the QP energy at $T = 0$ K and the eigenenergy at ground-state atomic positions (at the DFT level). The ZPR correction to the DFT band gap is found to be around 15–16 meV for LiZnAs and 36–39 meV for ScAgC. As shown in Fig. 1, this correction in LiZnAs is entirely accounted by a decrease in the conduction band minima (CBM) in both approaches, while a $\sim 31\text{--}33$ meV correction in the CBM is observed for ScAgC. This indicates that a large self-energy correction in the CBM at 0 K is present in both hH materials. Furthermore, the T-dependent energy of the CBM decreases linearly with increasing T in both materials. However, the valence band maximum (VBM) energy increases with T in LiZnAs, whereas the opposite behavior is observed in ScAgC, where the VBM energy decreases with T increases. A larger spectral weight transfer is observed at higher T compared to lower ones, possibly due to enhanced lattice scattering at higher T. However, at a given T, the amount of this weight transfer is smaller in LiZnAs than in ScAgC, indicating comparatively weaker *e-ph* scattering at the Γ -point in LiZnAs.

B. Charge carrier mobility

The mobility of charge carriers is one of the most important quantities for any semiconducting material, determining its suitability for applications in a wide variety of electronic and optoelectronic devices. Therefore, accurately determining the mobility is a key task, which requires extensive sampling of electron and phonon wave vectors in Brillouin zone. The results obtained for phonon-limited electron and hole mobilities

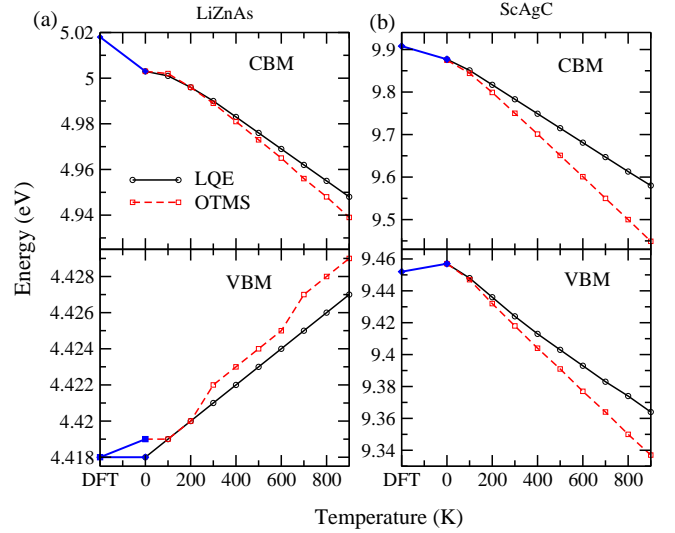


FIG. 1. Renormalization and temperature dependence of the VBM and CBM states at the Γ point obtained from both LQE and OTMS methods for (a) LiZnAs and (b) ScAgC. The blue lines indicate the ZPR, connecting the DFT eigenvalues with the renormalized energy at 0 K.

TABLE I. DFT band gap (without EPR), and ZPR correction along with temperature-dependent variations of the band gap obtained using the linearized quasiparticle equation (LQE) and on-the-mass-shell (OTMS) methods. All values are in eV.

Temperature (in K)	LiZnAs		ScAgC	
	LQE	OTMS	LQE	OTMS
ZPR	-0.015	-0.016	-0.036	-0.039
Without EPR	0.600	0.600	0.456	0.456
0	0.585	0.584	0.420	0.417
100	0.583	0.582	0.403	0.396
200	0.577	0.576	0.381	0.366
300	0.569	0.567	0.358	0.332
400	0.561	0.558	0.335	0.297
500	0.553	0.549	0.312	0.260
600	0.545	0.539	0.288	0.224
700	0.537	0.529	0.264	0.187
800	0.529	0.519	0.239	0.150
900	0.521	0.510	0.216	0.112

(μ_e and μ_h) using very fine sampling in both hH compounds are presented in Fig. 2. It is important to note in both materials that the μ_e is significantly higher than the μ_h . Both mobilities decrease with increasing T due to enhanced phonon scattering at higher T. At room-temperature, the obtained μ_e values for LiZnAs are $\sim 6500, 12560$, and $17000 \text{ cm}^2 \text{ V}^{-1} \text{ s}^{-1}$, as calculated using SERTA, MRTA and IBTE, respectively. These respective methods estimate μ_h values as $\sim 160, 213$, and $195 \text{ cm}^2 \text{ V}^{-1} \text{ s}^{-1}$. This μ_e result compares well with reported μ_e values for GaAs (a similar compound in terms of band structure), which range from 7000 to $12000 \text{ cm}^2 \text{ V}^{-1} \text{ s}^{-1}$ [52]. Furthermore, the room-temperature μ_e (μ_h) values for ScAgC are determined to be ~ 4010 (50), 9440 (70), and 8510

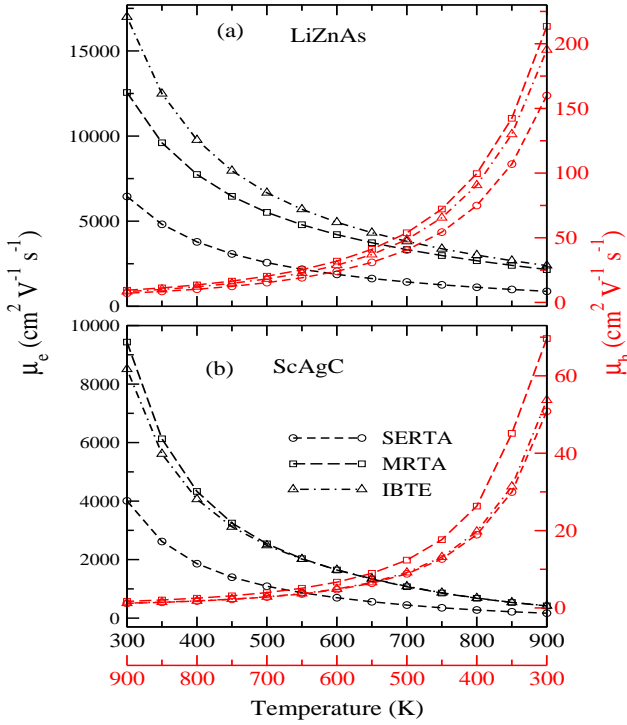


FIG. 2. Temperature-dependent electron and hole mobilities (μ_e and μ_h) using methods based on linearized (SERTA, MRTA) and iterative Boltzmann transport equation (IBTE) for (a) LiZnAs and (b) ScAgC.

(54) from respective methods. For both compounds, it can be observed that the MRTA-driven values are greater than or equal to the SERTA-based values across the studied T range, as expected due to the additional velocity factor in the MRTA framework.

In LiZnAs, the SERTA-driven μ_e values underestimate the exact solution in studied T range, while underestimation of μ_h values decreases with increasing T and becomes nearly the same at 900 K. Interestingly, MRTA gives lower values of μ_e than the IBTE-derived values, while opposite behavior (at-least below 600 K) is observed for the μ_h computation. At higher T, all three methods provide almost similar μ_h values, which means second term of Eq. (3) has a negligible contribution as the T increases, and the forward scattering also becomes nearly equal to the backward scattering around the band gap region of the valence band in LiZnAs.

In ScAgC, the MRTA and IBTE solutions provide almost identical μ_e values, especially beyond 400 K, that means velocity factor compensates the effect of the second term of Eq. (3) in the conduction band region around band gap. While result of μ_h observes the completely opposite behavior where the SERTA and IBTE methods give the almost same values, indicating that the hole-like region is not significantly influenced by the second term of Eq. (3). However, the velocity factor affects the values, and its impact decreases as the T increases. Finally, this study provides an upper bound for both mobilities limited by the e - ph coupling in these hH semiconductors. These results indicate that electron transport significantly outperforms hole transport, suggesting that n-type samples of both

materials can exhibit superior TE performance.

C. Thermoelectric transport properties

TE transport properties have been obtained using Boltzmann transport theory. The most commonly used approximation in this theory for calculating all three electrical properties (S , σ , and κ_e) is the CRTA, which assumes an energy-independent electron lifetime [30]. However, in semiconductors, due to the strong dependence of the electron lifetime on the electronic eigenvalues, CRTA can be an inadequate approach [30]. This inadequacy is often reflected in the significant discrepancies observed between CRTA-based results and experimental data [37, 61]. Therefore, it is crucial to account for intrinsic scattering phenomena to achieve accurate transport predictions, and in this work, a more demanding first principles e - ph coupling is considered [27]. Accordingly, we have analyzed and compared the electrical transport properties obtained using CRTA with those obtained via EPI-based SERTA and MRTA schemes. In this study, the transport properties under the CRTA are estimated using the BoltzTraP code [62]. To enable a clear comparison between the CRTA and EPI-based methods, the required electron-energy independent lifetime in CRTA is set equal to the value obtained from e - ph scattering (here, taken from MRTA) at a given T. In this context, the effects of e - ph scattering, or equivalently carrier lifetimes, are reflected through variations in carrier concentrations in the SERTA or MRTA approaches. All three electrical transport coefficients are calculated using the G_0W_0 band gap values (applied via scissor correction), which have been estimated in our previous study to be approximately 1.5 eV for LiZnAs and 1.0 eV for ScAgC [60]. Given that the μ_e is approximately 80–100 times higher than the μ_h (see Fig. 2), our investigation focuses only on the n-type case to research their TE properties, where enhanced efficiency is anticipated.

We begin by analyzing the Seebeck coefficients (S) for both n-type samples calculated using the CRTA, SERTA, and MRTA methods, which are plotted in Fig. 3 as a function of electron doping concentration (n_e) at 300, 600, and 900 K. It is clearly demonstrated for both materials that the physical behavior of S appears counterintuitive when relying solely on the CRTA framework. However, both SERTA and MRTA provide nearly similar S values, indicating that the average change of electron velocity during scattering processes in Eq. (4) is negligibly small when S is computed. The magnitude of S ($-S-$) increases with T and decreases with increasing n_e at a given T, analogous to a typical behavior of most semiconducting TE compounds. Since lifetime is assumed to be constant in CRTA, the value of S is not significantly improved with increasing concentration, which can also be due to the large band gap of these hH materials. Inclusion of e - ph scattering leads to a noticeable improvements in S across all T when compared to CRTA estimates, with the most significant enhancements observed at lower doping concentrations. Specifically, at a n_e value of 10^{17} cm^{-3} , S values are 2-6 times higher than those predicted by CRTA in both materials. However, this discrepancy decreases as n_e increases.

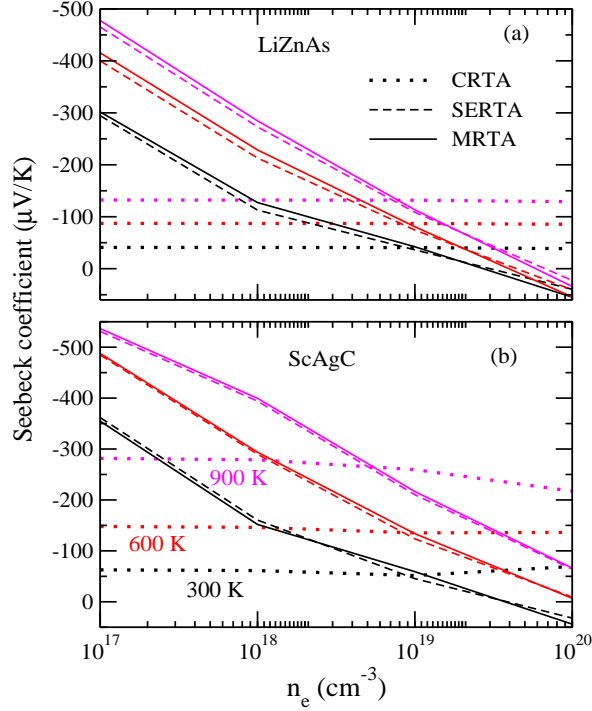


FIG. 3. The Seebeck coefficients of n-type of (a) LiZnAs and (b) ScAgC hH materials at different temperatures and increasing electron doping concentrations (n_e), calculated using the CRTA, SERTA and MRTA approaches.

Furthermore, S at the CRTA level is estimated to be always negative for both n-types LiZnAs and ScAgC, in line with conventional expectations. The EPI-based results, which take into account the e - ph scattering within the SERTA (or MRTA), reveal a sign reversal in S , becoming positive at large enough electron doping levels (10^{20} cm^{-3}) for LiZnAs at all T , and for ScAgC at 300 K. This type of sign-change behavior at high doping concentrations has also been observed in other hH material, such as TaFeSb [63]. This unusual trend arises from carrier scattering events between various electronic states, governed by their energy-dependent interactions. This highlights the importance of incorporating advanced scattering mechanisms to accurately capture carrier transport in typical TE materials [63]. The calculated S values are higher in ScAgC than in LiZnAs, which can be attributed to the less dispersive electronic bands in ScAgC compared to those in LiZnAs [60]. For instance, the $-S$ for LiZnAs at $n_e \sim 10^{18} \text{ cm}^{-3}$ are in the range of 113 to $285 \mu\text{VK}^{-1}$ within both EPI-based approaches, as T increases from 300 to 900 K. Whereas ScAgC exhibits a higher $-S$ range of 160 to $400 \mu\text{VK}^{-1}$ over the same T interval. This high- T value for ScAgC is comparable to that of the highly efficient TaFeSb material [63]. It has been observed in many n-type hH that high TE performance (zT) is typically associated with S in the range of -200 to $250 \mu\text{VK}^{-1}$ [9]. Therefore, both LiZnAs and ScAgC demonstrate promising characteristics for mid- and high- T TE applications.

Next the electrical conductivity (σ) is shown in Fig. 4. It is observed to show a decreasing trend of σ with increasing T

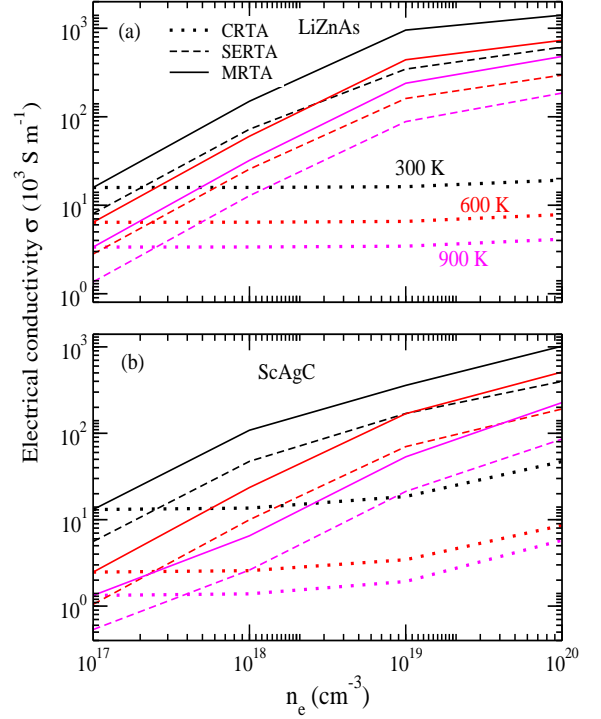


FIG. 4. Electrical conductivity of n-type of (a) LiZnAs and (b) ScAgC hH materials at different temperatures and increasing electron doping concentrations (n_e), calculated using CRTA, SERTA and MRTA.

at a fixed concentration, consistent with the change of μ_e with T , which is expected due to enhanced e - ph scattering at higher T . Due to the electron energy-independent lifetime in CRTA, the σ value does not significantly improve with increasing n_e , as seen in both materials. However, after considering the electronic state-dependent lifetime τ_{nk}^0 within the EPI framework, σ increases linearly with rising n_e at a fixed T , despite the decreasing μ_e [see Eq. (5)], likely due to the enhanced electronic density of states around the bottommost conduction band region. This behavior follows the relation of electron relaxation time with T , as well as the general trend $\sigma \propto n_e$. Thus, the strong energy dependence of lifetime reflects to a significant enhancement of σ at each T as doping density increases. At fixed T and n_e values, the MRTA-derived σ values are higher than those estimated using the SERTA calculations, indicating that the relative change in electron velocity during scattering cannot be neglected in the computation of σ . Finally, the highest obtained σ range of ~ 32125 - 479942 Sm^{-1} for LiZnAs using MRTA at 900 K across n_e range of 10^{18} - 10^{20} cm^{-3} is higher than that of ScAgC (~ 6500 - 226500 Sm^{-1}), as expected due to the larger μ_e in LiZnAs (see Fig. 2). Compared to other potential hH materials at high- T [9], these results clearly indicate the potential for achieving high TE performance in n-type LiZnAs and ScAgC.

The calculated κ_e for both n-type hH materials within CRTA, SERTA, and MRTA are plotted in Fig. 5, in which a similar trend of plots to that observed in σ is evident. A slight variation in the CRTA-predicted values with increasing n_e for all T values is seen for both compounds. However, a large

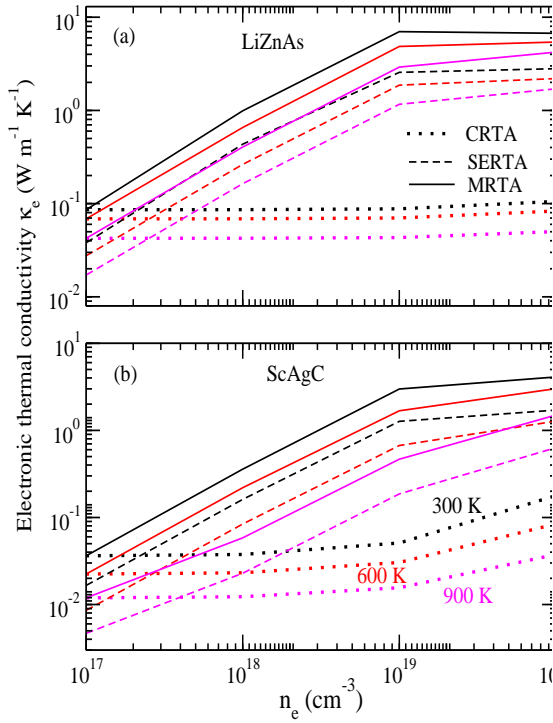


FIG. 5. Electronic thermal conductivity of n-type of (a) LiZnAs and (b) ScAgC hH materials at different temperatures and increasing electron doping concentrations (n_e), calculated using the CRTA, SERTA and MRTA approaches.

enhancement in κ_e occur when EPI scattering is included, as clearly observed in Fig. 5 for both materials. The increase in κ_e with n_e is a similar observation that has been observed in experimental studies. This marked change underscores the crucial role in between doping concentration and scattering interactions, which are inherently absent in the constant lifetime method. In the case of LiZnAs, SERTA- and MRTA-based all plots exhibit an initially linear increase in κ_e with n_e upto 10^{19} cm^{-3} , followed by a modest enhancement at high doping levels. However, for ScAgC, κ_e shows a more linear relationship with increasing T across the studied doping concentration range. It is also observed in both materials that the κ_e values from MRTA are more than twice as large as those calculated using SERTA. In general, lattice vibrations control most of the heat flow in semiconducting materials, therefore it is very crucial to understand the lattice transport for fully design and optimization of TE materials.

Therefore, the T -dependent κ_{ph} calculated from PPI for both considered materials is illustrated in Fig. 6. The calculated room-temperature values are ~ 5.5 and $7.4 \text{ W m}^{-1} \text{ K}^{-1}$ for LiZnAs and ScAgC, respectively. These values are further reduced as T increases due to enhanced phonon-phonon scattering, reaching ~ 1.8 and $2.4 \text{ W m}^{-1} \text{ K}^{-1}$, respectively, at 900 K. The calculated values for both hH materials at both temperatures are very similar to those of many high-performance hH materials [9], however they are also lower than those of many other hH materials (room-temperature κ_{ph} between 10 – $35 \text{ W m}^{-1} \text{ K}^{-1}$ [9, 64, 65]).

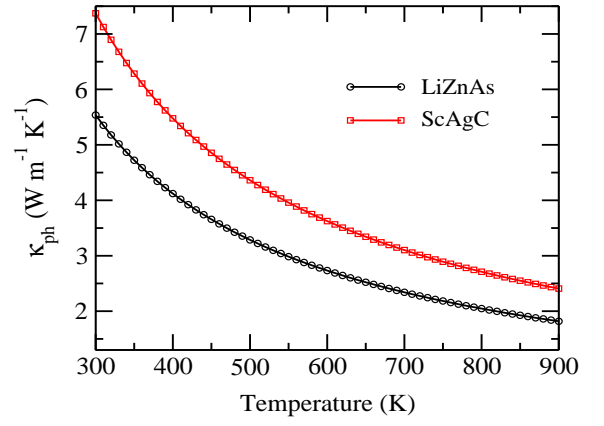


FIG. 6. Temperature-dependent lattice thermal conductivity (κ_{ph}).

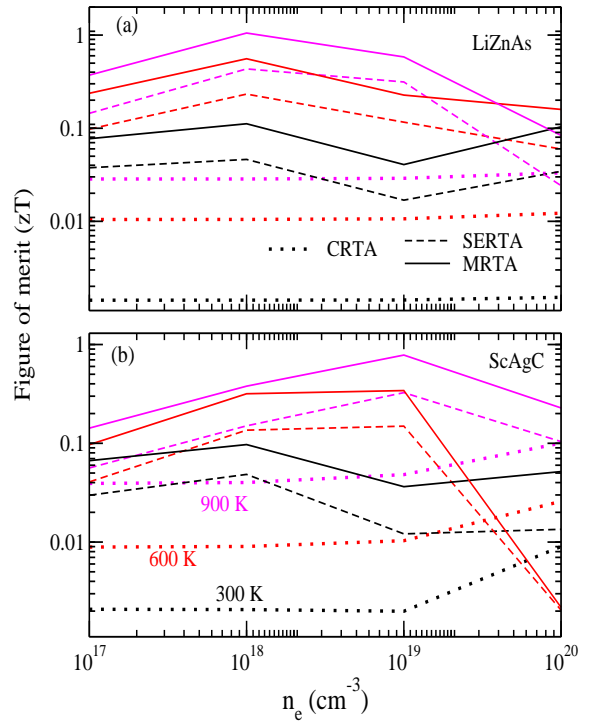


FIG. 7. Figure of merit (zT) of n-type of (a) LiZnAs and (b) ScAgC hH materials at different temperatures and increasing electron doping concentrations (n_e), calculated using CRTA, SERTA and MRTA.

Now based on the calculated electron transport coefficients and κ_{ph} , the TE performance (zT) for both hH materials has been obtained and is presented in Fig. 7. In this figure, one can clearly observe significant differences in the zT values derived from the CRTA and EPI-based approaches. For example, the highest zT for LiZnAs is obtained as ~ 1.05 and 0.44 using MRTA and SERTA, respectively, at a T value of 900 K for a 10^{18} cm^{-3} electron doping. In comparison, the corresponding values for ScAgC are ~ 0.78 and 0.33 at a similar T but for a 10^{19} cm^{-3} doping concentration. These values are almost 15–35 times larger than the CRTA-based estimations for LiZnAs and around 7–16 times higher in ScAgC. This large discrepancy

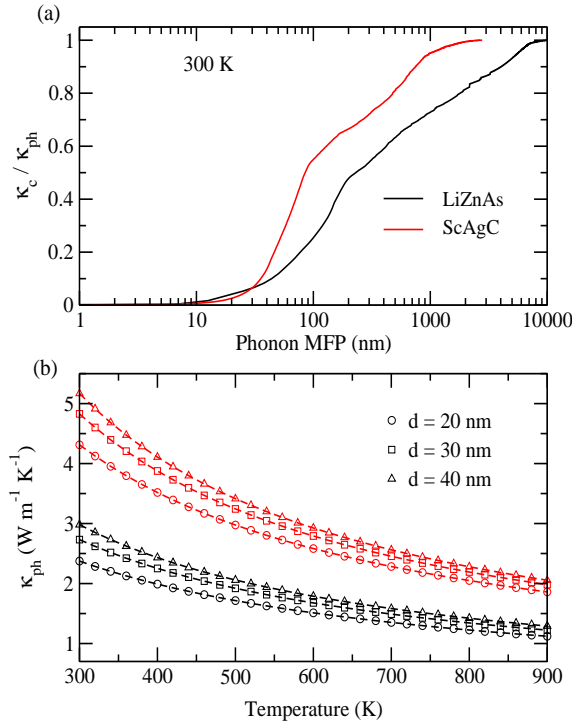


FIG. 8. (a) Normalized cumulative lattice thermal conductivity (κ_c/κ_{ph}) at room-temperature as a function of phonon mean-free path (MFP). (b) Temperature dependence of κ_{ph} by also including phonon boundary scattering using several grain sizes $d = 20, 30$, and 40 nm.

any in the zT results arises mainly from significantly lower S and σ values predicted by the CRTA method. Although the κ_e is lower within CRTA, this reduction does not sufficiently compensate the former reduction, resulting in overall lower zT values compared to those from EPI-based methods. This comparative analysis clearly highlights the significant impact of methodological choices on accurate zT predictions, underscoring the importance of careful consideration when interpreting and applying these results to the final performance evaluation of hH materials.

As discussed in the introduction section, due to the interrelation between electron transport coefficients, reducing κ_{ph} is a more efficient way to increase the performance of TE materials. This can be reduced by controlling the lattice transport without largely affecting the electron transport. The grain boundaries are commonly found in experimental samples and thus act as additional sources of scattering centers. Therefore, an effective approach to modulate transport behavior in materials is nanostructuring, which affects transport by causing scattering of carriers at grain boundaries [23, 35, 66, 67]. The transport of both particles significantly depends on the size of grain or nanostructure. The grain size can be selected by understanding the mean-free-path (MFP) distributions of both types of particles. The electron MFPs are much shorter than phonon MFPs in semiconductors [35], thus nanograins of moderate size can effectively block lattice heat conduction while having minimum impact on electrical transport. This approach has been seen for lowering κ_{ph} in semiconductors when the size

of nanostructures is chosen in the range of 10-100 nanometers (nm) [35, 68].

To support the proper selection of nanograin size, the room-temperature cumulative lattice thermal conductivity is analyzed and presented in Fig. 8(a), normalized by the bulk κ_{ph} value (κ_c/κ_{ph}) for these hH materials. It can be observed for both materials that phonons with MFPs below 10 nm contribute very little to heat conduction at 300 K. However, κ_{ph} receives significant contributions from phonons with MFPs upto almost $3 \mu\text{m}$ (for ScAgC) and $9 \mu\text{m}$ (for LiZnAs). It has been observed in most semiconductors that the large part of electron transport properties such as μ_e and σ [35, 37, 69] are decided by electron with MFPs shorter than 10 nm. This suggests that one can safely choose the grain size above 10 nm in both hH materials, as it would effectively scatter phonons without significantly affecting electron transport.

Therefore, we have selected various grain sizes to study the effect of nanostructuring on the κ_{ph} value. In this study, the nanograins size $d = 10, 20$, and 30 nm have been chosen, and the resulting κ_{ph} plots for both nanograined hH materials are shown in Fig. 8(b). This nanoinclusions effect in the calculation is considered in terms of the phonon-boundary scattering, using boundary scattering rates as v_g/d , where v_g is the phonon group velocity and d is the boundary MFP (or grain size). For both materials, the bulk κ_{ph} value decreases as the d value is reduced from 40 nm to 20 nm, which is expected due to enhanced boundary scattering at smaller grain size. For instance, the room-temperature bulk κ_{ph} for LiZnAs of $5.5 \text{ W m}^{-1} \text{K}^{-1}$ reduces to be $\sim 3, 2.7$, and $2.4 \text{ W m}^{-1} \text{K}^{-1}$ for d values of $40, 30$, and 20 nm, respectively. Similarly, the value of $7.4 \text{ W m}^{-1} \text{K}^{-1}$ for ScAgC is reduced to be $\sim 5.2, 4.8$, and $4.3 \text{ W m}^{-1} \text{K}^{-1}$ for the respective d values. However, in both materials, the differences in κ_{ph} values among these d values become very little at higher T , indicating that phonon-boundary scattering becomes less effective as T increases.

Using these nanograined sample values, we further calculate the zT values. A strong impact of nanostructuring is observed on these hH materials' performance. For example, the highest zT for LiZnAs obtained at 900 K and 10^{18} cm^{-3} concentration, 1.05 using MRTA, largely increases to $\sim 1.53, 1.44$, and 1.38 for d values of $20, 30, 40$ nm, respectively. At these respective d values, the increase from the value of 0.78 for 10^{19} cm^{-3} concentration in ScAgC is observed to be $\sim 1.0, 0.92$, and 0.9 . These results indicate that, due to nanostructure technique, the highest zT value at high- T is increased by almost 50% in LiZnAs and 25% in ScAgC with a 20 nm nanograin size. Such a substantial enhancement shows the major significance of nanostructuring techniques in predicting high-performance TE materials.

Finally, in our previous study [60], both hH materials have been predicted to be good solar cell materials, exhibiting high efficiencies (greater than 30%) in single-junction solar cells. Since the LiZnAs compound has already been prepared experimentally [60], the successful fabrication of ScAgC could also prove beneficial for energy-related applications. Therefore, both hH materials hold promise as multifunctional candidates, capable of efficient performance in both solar cell and TE technologies.

IV. CONCLUSIONS

In summary, we have employed comprehensive *ab initio* MBPT calculations based on DFT and DFPT to investigate the impact of *e-ph* coupling on the electronic band structure, electrical carrier mobilities, and thermoelectric transport coefficients of LiZnAs and ScAgC compounds. All relevant quantities, including electronic and phononic eigenvalues, and *e-ph* matrix elements are estimated from first principles. The ZPR corrections of ~ 15 -16 and 36-39 meV to the KS band gap value of ~ 0.6 and 0.45 eV in LiZnAs and ScAgC, respectively, has been estimated using non-adiabatic AHC calculations. Furthermore, the electron transport properties are computed using BTE with various RTAs, including SERTA, MRTA and IBTE under EPI calculations. The μ_e values are significantly higher than the μ_h values over the T range of 300-900 K. The room-temperature μ_e (μ_h) values within EPI-based methods are obtained in the range of ~ 6500 -17000 (160 -213) $\text{cm}^2 \text{V}^{-1} \text{s}^{-1}$ in LiZnAs and ~ 4010 -8510 (50 -70) $\text{cm}^2 \text{V}^{-1} \text{s}^{-1}$ in ScAgC. All three electrical transport components of these TE materials obtained using CRTA over the electron concentration range of 10^{17} - 10^{20}cm^{-3} are significantly influ-

enced by the energy-dependent lifetimes within SERTA and MRTA, highlighting the dominant role of *e-ph* coupling in these hH materials. Furthermore, the κ_{ph} calculated using PPI is decreased through nanostructuring techniques, modeled via phonon-boundary scattering with varying grain sizes. Finally, the zT is obtained to be maximum with value of ~ 1.05 (0.78) for an electron concentration of 10^{18} (10^{19}) cm^{-3} at 900 K within MRTA for LiZnAs (ScAgC), and this value is increased to be ~ 1.53 (1.0) when a 20 nm nanograin is considered. These results clearly indicate the critical role of intrinsic electron-phonon, phonon-phonon, and phonon-boundary scattering mechanisms for accurately obtaining the highly efficient hH TE materials.

ACKNOWLEDGEMENT

We acknowledge the computational support provided by the High-Performance Computing (HPC) PARAM Himalaya at the Indian Institute of Technology Mandi.

-
- [1] Z. Dong, J. Luo, C. Wang, Y. Jiang, S. Tan, Y. Zhang, Y. Grin, Z. Yu, K. Guo, J. Zhang, and W. Zhang, Half-Heusler-like compounds with wide continuous compositions and tunable p-to n-type semiconducting thermoelectrics, *Nat. Commun.* **13**, 35 (2022).
 - [2] J.-W. G. Bos and R. A. Downie, Half-Heusler thermoelectrics: a complex class of materials, *J. Phys.: Condens. Matter* **26**, 433201 (2014).
 - [3] T. Zhu, C. Fu, H. Xie, Y. Liu, and X. Zhao, High efficiency half-Heusler thermoelectric materials for energy harvesting, *Adv. Energy Mater.* **5**, 1500588 (2015).
 - [4] H. Zhu, W. Li, A. Nozariasbmarz, N. Liu, Y. Zhang, S. Priya, and B. Poudel, Half-Heusler alloys as emerging high power density thermoelectric cooling materials, *Nat. Commun.* **14**, 3300 (2023).
 - [5] C. Fu, T. Zhu, Y. Liu, H. Xie, and X. Zhao, Band engineering of high performance p-type FeNbSb based half-Heusler thermoelectric materials for figure of merit $zT_{1/2}$, *Energy Environ. Sci.* **8**, 216 (2015).
 - [6] C. Fu, S. Bai, Y. Liu, Y. Tang, L. Chen, X. Zhao, and T. Zhu, Realizing high figure of merit in heavy-band p-type half-Heusler thermoelectric materials, *Nat. Commun.* **6**, 8144 (2015).
 - [7] J. Yang, H. Li, T. Wu, W. Zhang, L. Chen, and J. Yang, Evaluation of half-Heusler compounds as thermoelectric materials based on the calculated electrical transport properties, *Adv. Funct. Mater.* **18**, 2880 (2008).
 - [8] G. Samsonidze and B. Kozinsky, Accelerated screening of thermoelectric materials by first-principles computations of electron-phonon scattering, *Adv. Energy Mater.* **8**, 1800246 (2018).
 - [9] G. Rogl and P. F. Rogl, Development of thermoelectric half-Heusler alloys over the past 25 years, *Crystals* **13**, 1152 (2023).
 - [10] S. S. Shastri and S. K. Pandey, Theory of energy conversion between heat and electricity, in *Thermoelectricity and Advanced Thermoelectric Materials*, Woodhead Publishing Series in Elec-
 - tronic and Optical Materials, edited by R. Kumar and R. Singh (Woodhead Publishing, Duxford, 2021) pp. 21–53.
 - [11] C. Uher, J. Yang, S. Hu, D. T. Morelli, and G. P. Meisner, Transport properties of pure and doped MNiSn (M=Zr, Hf), *Phys. Rev. B* **59**, 8615 (1999).
 - [12] S. S. Shastri and S. K. Pandey, Thermoelectric properties, efficiency and thermal expansion of Zr-NiSn half-Heusler by first-principles calculations, *J. Phys.: Condens. Matter* **32**, 355705 (2020).
 - [13] M. Zeeshan, H. K. Singh, J. van den Brink, and H. C. Kandpal, Ab initio design of new cobalt-based half-Heusler materials for thermoelectric applications, *Phys. Rev. Mater.* **1**, 075407 (2017).
 - [14] T. Graf, C. Felser, and S. S. P. Parkin, Simple rules for the understanding of Heusler compounds, *Prog. Solid State Chem.* **39**, 1 (2011).
 - [15] J. Carrete, W. Li, N. Mingo, S. Wang, and S. Curtarolo, Finding unprecedentedly low-thermal-conductivity half-Heusler semiconductors via high-throughput materials modeling, *Phys. Rev. X* **4**, 011019 (2014).
 - [16] F. Casper, T. Graf, S. Chadov, B. Balke, and C. Felser, Half-Heusler compounds: novel materials for energy and spintronic applications, *Semicond. Sci. Technol.* **27**, 063001 (2012).
 - [17] W. Xie, A. Weidenkaff, X. Tang, Q. Zhang, J. Poon, and T. M. Tritt, Recent advances in nanostructured thermoelectric half-Heusler compounds, *Nanomaterials* **2**, 379 (2012).
 - [18] D. Beretta, N. Neophytou, J. M. Hodges, and et al., Thermoelectrics: From history, a window to the future, *Mater. Sci. Eng. R Rep.* **138**, 100501 (2019).
 - [19] V. Pecunia, S. R. P. Silva, J. D. Phillips, and et al., Roadmap on energy harvesting materials, *J. Phys. Mater.* **6**, 042501 (2023).
 - [20] S. Sakurada and N. Shutoh, Effect of Ti substitution on the thermoelectric properties of (Zr,Hf)NiSn half-Heusler compounds, *Appl. Phys. Lett.* **86**, 082105 (2005).

- [21] S. Liu, Y. Hu, S. Dai, Z. Dong, G. Wu, J. Yang, and J. Luo, Synergistically optimizing electrical and thermal transport properties of ZrCoSb through Ru doping, *ACS Appl. Energy Mater.* **4**, 13997 (2021).
- [22] R. Tranås, O. M. Løvvik, and K. Berland, Attaining low lattice thermal conductivity in Half-Heusler sublattice solid solutions: Which substitution site is most effective?, *Electron. Mater.* **3**, 1 (2022).
- [23] G. Joshi, X. Yan, H. Wang, W. Liu, G. Chen, and Z. Ren, Enhancement in thermoelectric figure-of-merit of an n-type half-Heusler compound by the nanocomposite approach, *Adv. Energy Mater.* **1**, 643 (2011).
- [24] J. Park, A. M. Ganose, and Y. Xia, Advances in theory and computational methods for next-generation thermoelectric materials, *Appl. Phys. Rev.* **12**, 011339 (2025).
- [25] N. W. Ashcroft and N. D. Mermin, *Solid State Physics* (Holt, Rinehart and Winston, New York, 1976).
- [26] M. Bernardi, First-principles dynamics of electrons and phonons, *Eur. Phys. J. B* **89**, 1 (2016).
- [27] J. Zhou, B. Liao, and G. Chen, First-principles calculations of thermal, electrical, and thermoelectric transport properties of semiconductors, *Semicond. Sci. Technol.* **31**, 043001 (2016).
- [28] S. Poncé, W. Li, S. Reichardt, and F. Giustino, First-principles calculations of charge carrier mobility and conductivity in bulk semiconductors and two-dimensional materials, *Rep. Prog. Phys.* **83**, 036501 (2020).
- [29] F. Giustino, Electron-phonon interactions from first principles, *Rev. Mod. Phys.* **89**, 015003 (2017).
- [30] J. M. Ziman, *Electrons and Phonons: The Theory of Transport Phenomena in Solids* (Clarendon Press, Oxford, 1960).
- [31] F. Giustino, S. G. Louie, and M. L. Cohen, Electron-phonon renormalization of the direct band gap of diamond, *Phys. Rev. Lett.* **105**, 265501 (2010).
- [32] G. Antonius, S. Poncé, P. Boulanger, M. Côté, and X. Gonze, Many-body effects on the zero-point renormalization of the band structure, *Phys. Rev. Lett.* **112**, 215501 (2014).
- [33] S. Poncé, Y. Gillet, J. Laflamme Janssen, A. Marini, M. Verstraete, and X. Gonze, Temperature dependence of the electronic structure of semiconductors and insulators, *J. Chem. Phys.* **143**, 102813 (2015).
- [34] S. Poncé, J.-M. Lihm, and C.-H. Park, Verification and validation of zero-point electron-phonon renormalization of the bandgap, mass enhancement, and spectral functions, *npj Comput. Mater.* **11**, 117 (2025).
- [35] B. Qiu, Z. Tian, A. Vallabhaneni, B. Liao, J. M. Mendoza, O. D. Restrepo, X. Ruan, and G. Chen, First-principles simulation of electron mean-free-path spectra and thermoelectric properties in silicon, *EPL* **109**, 57006 (2015).
- [36] A. Minnich, M. S. Dresselhaus, Z. Ren, and G. Chen, Bulk nanostructured thermoelectric materials: current research and future prospects, *Energy Environ. Sci.* **2**, 466 (2009).
- [37] V. K. Solet and S. K. Pandey, Band gap renormalization, carrier mobility, and transport in Mg₂Si and Ca₂Si: *Ab initio* scattering and Boltzmann transport equation study, *Phys. Rev. B* **111**, 205203 (2025).
- [38] R. Gautier, X. Zhang, L. Hu, L. Yu, Y. Lin, T. O. Sunde, D. Chon, K. R. Poepplmeier, and A. Zunger, Prediction and accelerated laboratory discovery of previously unknown 18-electron ABX compounds, *Nature Chem* **10.1038/nchem.2207**.
- [39] Y. O. Ciftci and S. D. Mahanti, Electronic structure and thermoelectric properties of half-Heusler compounds with eight electron valence count—KScX (X= C and Ge), *J. Appl. Phys.* **119**, 145703 (2016).
- [40] J. Barth, G. H. Fecher, M. Schwind, A. Beleanu, C. Felser, A. Shkabko, A. Weidenkaff, J. Hanss, A. Reller, and M. Köhne, Investigation of the thermoelectric properties of LiAlSi and LiAlGe, *J. Electron. Mater.* **39**, 1856 (2010).
- [41] Vikram, B. Sahni, C. K. Barman, and A. Alam, Accelerated discovery of new 8-electron half-Heusler compounds as promising energy and topological quantum materials, *J. Phys. Chem. C* **123**, 7074 (2019).
- [42] E. S. Toberer, A. F. May, C. J. Scanlon, and G. J. Snyder, Thermoelectric properties of p-type LiZnSb: Assessment of *ab initio* calculations, *J. Appl. Phys.* **105**, 063701 (2009).
- [43] V. K. Solet, S. Sk, and S. K. Pandey, First-principles study of optoelectronic and thermoelectronic properties of the ScAgC half-Heusler compound, *Phys. Scr.* **97**, 105711 (2022).
- [44] B. Sahni, Vikram, J. Kangsabanik, and A. Alam, Reliable prediction of new quantum materials for topological and renewable-energy applications: A high-throughput screening, *J. Phys. Chem. Lett.* **11**, 6364 (2020).
- [45] M. K. Yadav and B. Sanyal, First principles study of thermoelectric properties of Li-based half-Heusler alloys, *J. Alloys Compd.* **622**, 388 (2015).
- [46] A. Nazir, E. A. Khera, M. Manzoor, B. A. Al-Asbahi, and R. Sharma, Tunable opto-electronic and thermoelectric response of alkali based half-Heusler semiconductors AMgN (A= Rb, Cs) for sustainable energy: A computational approach, *MSEB* **303**, 117338 (2024).
- [47] A. Azouaoui, A. Hourmatallah, N. Benzakour, and K. Bouslykhane, First-principles study of optoelectronic and thermoelectric properties of LiCaX (X= N, P and As) half-Heusler semiconductors, *J. Solid State Chem.* **310**, 123020 (2022).
- [48] O. R. Jolayemi, B. I. Adetunji, O. E. Osafire, and G. A. Adebayo, Investigation of the thermoelectric properties of Lithium-Aluminium-Silicide (LiAlSi) compound from first-principles calculations, *Comput. Condens. Matter* **27**, e00551 (2021).
- [49] M. Fiorentini and N. Bonini, Thermoelectric coefficients of n-doped silicon from first principles via the solution of the Boltzmann transport equation, *Phys. Rev. B* **94**, 085204 (2016).
- [50] X. Gonze and C. Lee, Dynamical matrices, born effective charges, dielectric permittivity tensors, and interatomic force constants from density-functional perturbation theory, *Phys. Rev. B* **55**, 10355 (1997).
- [51] S. Baroni, S. de Gironcoli, A. Dal Corso, and P. Giannozzi, Phonons and related crystal properties from density-functional perturbation theory, *Rev. Mod. Phys.* **73**, 515 (2001).
- [52] G. Brunin, H. P. C. Miranda, M. Giantomassi, M. Royo, M. Stengel, M. J. Verstraete, X. Gonze, G.-M. Rignanese, and G. Hautier, Phonon-limited electron mobility in Si, GaAs, and GaP with exact treatment of dynamical quadrupoles, *Phys. Rev. B* **102**, 094308 (2020).
- [53] J. P. Perdew, K. Burke, and M. Ernzerhof, Generalized gradient approximation made simple, *Phys. Rev. Lett.* **77**, 3865 (1996).
- [54] X. Gonze, J.-M. Beuken, R. Caracas, F. Detraux, M. Fuchs, G.-M. Rignanese, L. Sindic, M. Verstraete, G. Zerah, F. Jollet, M. Torrent, A. Roy, M. Mikami, P. Ghosez, J.-Y. Raty, and D. C. Allan, First-principles computation of material properties: the ABINIT software project, *Comput. Mater. Sci.* **25**, 478 (2002).
- [55] X. Gonze, B. Amadon, G. Antonius, F. Arnardi, L. Baguet, J.-M. Beuken, J. Bieder, F. Bottin, J. Bouchet, E. Bousquet, N. Brouwer, F. Bruneval, G. Brunin, T. Cavignac, J.-B. Charraud, W. Chen, M. Côté, S. Cottenier, J. Denier, and G. Geneste *et al.*, The ABINIT project: Impact, environment and recent developments, *Comput. Phys. Commun.* **248**, 107042 (2020).

- [56] S. Poncé, G. Antonius, Y. Gillet, P. Boulanger, J. Laflamme Janssen, A. Marini, M. Côté, and X. Gonze, Temperature dependence of electronic eigenenergies in the adiabatic harmonic approximation, *Phys. Rev. B* **90**, 214304 (2014).
- [57] S. Poncé, G. Antonius, P. Boulanger, E. Cannuccia, A. Marini, M. Côté, and X. Gonze, Verification of first-principles codes: Comparison of total energies, phonon frequencies, electron–phonon coupling and zero-point motion correction to the gap between ABINIT and QE/Yambo, *Computational Materials Science* **83**, 341 (2014).
- [58] A. Togo, L. Chaput, and I. Tanaka, Distributions of phonon lifetimes in Brillouin zones, *Phys. Rev. B* **91**, 094306 (2015).
- [59] V. K. Solet and S. K. Pandey, Ab initio study of phononic thermal conduction in ScAgC half-Heusler, *Eur. Phys. J. B* **96**, 53 (2023).
- [60] V. K. Solet and S. K. Pandey, Many-body *ab initio* study of quasiparticles, optical excitations, and excitonic properties in LiZnAs and ScAgC for photovoltaic applications, *Phys. Rev. Appl.* **23**, 064040 (2025).
- [61] H. N. Nam, K. Suzuki, T. Q. Nguyen, A. Masago, H. Shinya, T. Fukushima, and K. Sato, Low-temperature acanthite-like phase of Cu₂S: Electronic and transport properties, *Phys. Rev. B* **105**, 075205 (2022).
- [62] G. K. Madsen and D. J. Singh, BoltzTraP. A code for calculating band-structure dependent quantities, *Comput. Phys. Commun.* **175**, 67 (2006).
- [63] N. S. Fedorova, A. Cepellotti, and B. Kozinsky, Anomalous thermoelectric transport phenomena from first-principles computations of interband electron–phonon scattering, *Adv. Funct. Mater.* **32**, 2111354 (2022).
- [64] A. N. Gandi and U. Schwingenschlögl, Thermoelectric properties of the XCoSb (X: Ti, Zr, Hf) Half-Heusler alloys, *Phys. Status Solidi B* **254**, 1700419 (2017).
- [65] S. S. Shastri and S. K. Pandey, First-principles electronic structure, phonon properties, lattice thermal conductivity and prediction of figure of merit of FeVSb half-Heusler, *J. Phys. Condens. Matter* **33**, 085704 (2020).
- [66] A. J. Minnich, H. Lee, X. W. Wang, G. Joshi, M. S. Dresselhaus, Z. F. Ren, G. Chen, and D. Vashaee, Modeling study of thermoelectric SiGe nanocomposites, *Phys. Rev. B* **80**, 155327 (2009).
- [67] M. S. Dresselhaus, G. Chen, M. Y. Tang, R. Yang, H. Lee, D. Wang, Z. Ren, J.-P. Fleurial, and P. Gogna, New directions for low-dimensional thermoelectric materials, *Adv. Mater.* **19**, 1043 (2007).
- [68] G. Chen, D. Borca-Tascuic, and R. G. Yang, Encyclopedia of nanoscience and nanotechnology, in *Encyclopedia of nanoscience and nanotechnology*, Vol. 7, edited by H. S. Nalwa (American Scientific Publishers, Valencia, CA, 2004) p. 429.
- [69] W. Li, Electrical transport limited by electron-phonon coupling from Boltzmann transport equation: An ab initio study of Si, Al, and MoS₂, *Phys. Rev. B* **92**, 075405 (2015).